Chem. Mater. **2006,** *18,* 804−813

Electrochemical, Magnetic, and Structural Investigation of the $Li_x(Mn_yFe_{1-y})PO_4$ Olivine Phases

Atsuo Yamada,* Yuki Takei, Hiroshi Koizumi, Noriyuki Sonoyama, and Ryoji Kanno

Department of Electronic Chemistry, Interdisciprinary Graduate School of Science and Engineering, Tokyo Institute of Technology, 4259 Nagatsuta, Midori, Yokohama, 226-8502 Japan

Keiji Itoh

Research Reactor Institute, Kyoto University, Kumatori-cho, Senna-gun, 590-0494 Japan

Masao Yonemura and Takashi Kamiyama

Institute of Materials Structure Science, High Energy Accelerator Research Organization, 1-1 Oho, Tsukuba, 305-0801 Japan

Received August 18, 2005. Revised Manuscript Received December 7, 2005

A series of synthetic heterosite−purpurite, $(Mn_yFe_{1-y})PO_4$ ($y < 0.8$), with negligible disorder and impurities, was obtained by chemical oxidation of the well-crystallized isotypic tryphillite−lithiophilite series, $Li(Mn_yFe_{1-y})PO_4$ (ordered olivine structure, space group *Pnma*). Comparative magnetic and X-ray/neutron powder diffraction investigations of the two solid−solution lines were performed as a function of Mn content to increase understanding of the electrochemical activity loss of Mn^{3+}/Mn^{2+} in the $Li_x(Mn_yFe_{1-y})PO_4$ electrode system. Introducing Mn ions into the 4c site did not cause significant change in the local geometry of $M^{2+}O_6$ and PO_4 polyhedra, while the $M^{3+}O_6$ octahedra became severely distorted with an increase in the number of Jahn−Teller active Mn^{3+} ions. The edge-sharing geometry of $M^{3+}O_6$ and PO_4 polyhedra fixed the shared O3′−O3′ interatomic distance, causing selective strong elongation of the M^{3+}−O3′ distance with small shrinkage of other M^{3+}−O1, M^{3+}−O2, and M^{3+}−O3 bond lengths. The overall distortion of the MO_6 octahedra with $M = Mn^{3+}$ was much larger than the corresponding change in the unit-cell orthorombicity and significantly increased asymmetry in the M−O−M superexchange interaction. All samples exhibited antiferromagnetism; however, the trivalent series had more than a sevenfold larger decrease in Neel temperature T_N (from ca. 130 K at $y = 0$ to ca. 50 K at $y = 0.8$) compared to the divalent series (from ca. 52 K at $y = 0$ to ca. 35 K at $y = 1$) as a function of the Mn content y.

Introduction

$LiFePO_4$ (triphylite) and $LiMnPO_4$ (lithiophilite), the lithium orthophosphates of divalent iron and manganese, form a solid−solution series isomorphous with olivine having an orthorhombic unit cell with four formula units and space group *Pnma* (see Figure 1). The olivine-type structure contains a distorted hexagonal close-packing of oxygen anions, with three types of cations occupying the interstitial sites: (i) corner-sharing MO_6 (M = transition metals) octahedra, which are nearly coplanar to form a distorted two-dimensional square lattice perpendicular to the *a* axis; (ii) edge-sharing LiO_6 octahedra aligned in parallel chains along the *b* axis; and (iii) tetrahedral PO_4 groups connecting neighboring planes or arrays.

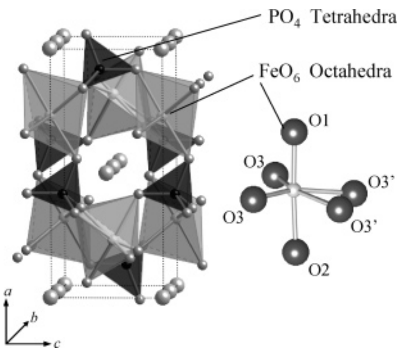

Figure 1. Crystal structure of $LiFePO_4$ and local geometry of the FeO_6 octahedra. Note that the axial direction in FeO_6 octahedra is not parallel to the orthorhombic axis.

This class of compounds, particularly $LiFePO_4$, has been studied intensively because of low cost, nontoxicity, and superb thermal stability that allow the construction of rechargeable lithium battery electrodes for use in large-scale applications such as electric/hybrid vehicles and load leveling systems.[1] The Fe^{3+}/Fe^{2+} redox reaction in Li_xFePO_4 generates 3.4 V versus Li/Li^+ with a theoretical capacity of 170 mA·h/g, most of which can be delivered in the optimized electrode powder, and yield a large energy density competitive with those of conventional Li_xCoO_2 cathodes.[2] Substantial improvements in the cathode activity of $LiFePO_4$ have

---

* To whom correspondence should be addressed. E-mail: yamada@echem.titech.ac.jp.

(1) Padhi, A. K.; Nanjundaswamy, K. S.; Goodenough, J. B. *J. Electrochem. Soc.* **1997**, *144*, 1188.

(2) Yamada, A.; Chung, S.-C.; Hinokuma, K. *J. Electrochem. Soc*. **2001**, *148*, A224.

10.1021/cm051861f CCC: $33.50

been achieved by carbon nanopainting,[3−6] particle size minimization,[2] and supervalent cation doping into the Li 4a site or carbothermal formation of the surface conducting phases,[7,8] which counteract the low inherent electronic conductivity.

The Mn^{3+}/Mn^{2+} redox couple in the olivine framework is positioned at 4.1 V versus Li/Li^+ but possesses much slower kinetics compared to Fe^{3+}/Fe^{2+}.[1,9−11] Despite the higher open circuit voltage (OCV), the current durability in Li_xMnPO_4 is orders of magnitude lower than that in Li_xFePO_4, and the effective energy density of $LiMnPO_4$ is much smaller than that of Li_xFePO_4.[12−14] This has led battery engineers to concentrate on improving $LiFePO_4$ rather than using the Mn^{3+}/Mn^{2+} redox couple in olivines; more than 170 papers on this subject have been published in the past four years. On the other hand, literature with promising perspectives for Li_xMnPO_4 cathodes is very limited.[15] In addition, the OCV of 3.4 V versus Li/Li^+ in Li_xFePO_4 provides a large overvoltage "margin" to oxidative electrolyte decomposition. Long-term stable operation and enhanced charging kinetics under acceptable anodic overvoltage are important technical advantages of Li_xFePO_4 cathodes.[16]

Reasons for the abnormally low electrochemical activity of the Mn^{3+}/Mn^{2+} redox couple have been examined using a $Li_x(Mn_yFe_{1-y})PO_4$ solid−solution system, which provides continuous parametric information between electrochemically active Li_xFePO_4 and inactive Li_xMnPO_4 phases.[9] Systematic identification of the redox chemistry and the general trend in the (x, y) two-dimensional phase diagram have been reported.[10,11] Mechanisms proposed to inactivate the Mn^{3+}/Mn^{2+} redox reaction, which are backed by experimental evidence, include (i) heavy polaronic holes localized on the Mn^{3+} sites;[11,12] (ii) a large kinetic barrier at the mismatched interface of $MnPO_4/LiMnPO_4$;[9,14] (iii) disordering or local phase segregation in the metastable $MnPO_4$ phase;[9,13] and (iv) the more than five orders of magnitude lower electronic conductivity of $LiMnPO_4$ compared to that of $LiFePO_4$ at room temperature, with a much higher binding energy (650−1000 meV vs 390−500 meV) of the polaron localization.[6,12,14,17]

The key aspect in this important class of materials is that the major structural anomalies, such as anisotropic deformation, significant loss of long-range order, and local phase segregation, have been detected in the phases with Mn^{3+}.[9,10,13] This is reasonable because Mn^{3+} is a typical Jahn−Teller ion, indicating the importance of the acquisition of accurate structural, magnetic, and transport data along the $(Mn_yFe_{1-y})PO_4$ solid−solution line for understanding the origin of the loss of electrochemical activity. However, previous studies have been limited to structural analyses of minerals (heterosite, $y \sim 1/3$; purpurite, $y \sim 2/3$), which usually present the specific manganese content with structural disorder and impurities due to their natural origin.[18] Difficulties in synthesizing phase-pure $Li(Mn_yFe_{1-y})PO_4$ and, hence, its oxidized form $(Mn_yFe_{1-y})PO_4$ also have been discussed in terms of the unexpected segregation of oxidized or reduced impurities.[2,8,19] Although recent studies demonstrate that pure $(Mn_yFe_{1-y})PO_4$ phases with any manganese content of $y < 0.8$ can be obtained by chemical delithation from high-quality synthetic $Li(Mn_yFe_{1-y})PO_4$, only the orthorhombic lattice dimensions were provided.[9] Systematic, accurate, and detailed structural and magnetic analyses on the synthetic phase-pure $Li(Mn_yFe_{1-y})PO_4$ and $(Mn_yFe_{1-y})PO_4$ solid solutions have to our knowledge not been documented before.

Experimental Section

Phase-pure $Li(Mn_yFe_{1-y})PO_4$ powders were synthesized by a solid-state reaction. A stoichiometric amount of lithium carbonate Li_2CO_3 (Wako, >99%), iron(II) oxalate dihydrate [$Fe(II)C_2O_4\cdot 2H_2O$, Aldrich, 99%], manganese(II) oxalate hemihydrate [$Mn(II)C_2O_4\cdot 0.5H_2O$, Wako, >99%], and diammonium hydrogen phosphate [$(NH_4)_2HPO_4$, Wako, >99%] were used as starting materials. A total of 10 g of raw materials was added to a 250-mL Cr-hardened SUS container with a mixture of 10 millimeters in diameter (mmϕ) $\times$ 10 and 5 mmϕ $\times$ 16 Cr-hardened SUS balls and thoroughly mixed by a conventional planetary milling apparatus for 6 h. The olivine phase was synthesized by sintering at 700 °C for 6 h in a purified Ar gas flow.

Chemical oxidation to obtain $(Mn_yFe_{1-y})PO_4$ was performed by reacting $Li(Mn_yFe_{1-y})PO_4$ with nitronium tetrafluoroborate (NO_2BF_4, Aldrich, >95%) in acetonitrile.[20] The redox potential of NO_2^+/NO_2 is about 5.1 V versus Li/Li^+, and it effectively oxidizes $Li(Mn_yFe_{1-y})PO_4$ with redox potentials of 3.4 V (Fe^{3+}/Fe^{2+}) and 4.1 V (Mn^{3+}/Mn^{2+}) versus Li/Li^+. After dissolving about 2 g of NO_2BF_4, twofold greater than the amount needed for the reaction, into 100 mL of acetonitrile, about 1 g of active material was added, and the mixture was stirred for 24 h at room temperature with bubbling of purified Ar gas. The products were filtered several times to remove impurities before drying under vacuum.

Diffraction patterns of the powdered samples were obtained with an X-ray diffractometer (Rigaku RAD-C, 12 kW) using Cu Kα

---

(3) Ravet, N.; Goodenough, J. B.; Besner, S.; Simoneau, M.; Hovington, P.; Armand, M. *The Electrochemical Society and the Electrochemical Society of Japan Meeting Abstracts*, Honolulu, HI, Oct 17−22, 1999; The Electrochemical Society, Inc.: Pennington, NJ, 1999; Abstract 127, Meeting 99-2.
(4) Huang, H.; Yin, S.-C.; Nazar, L. F. *Electrochem. Solid State Lett.* **2001**, *4*, A170.
(5) Chen, Z.; Dahn, J. R. *J. Electrochem. Soc.* **2002**, *149*, A1184.
(6) Yamada, A.; Hosoya, M.; Chung, S.-C.; Kudo, Y.; Hinokuma, K.; Liu, K.-Y.; Nishi, Y. *J. Power Sources* **2003**, *119−121*, 232.
(7) Chung, S. Y.; Bloking, J. T.; Chiang, Y. M. *Nat. Mater*. **2002**, *2*, 123.
(8) Herle, P. S.; Ellis, B.; Coombs, N.; Nazar, L. F. *Nat. Mater*. **2004**, *3*, 147.
(9) Yamada, A.; Chung, S.-C. *J. Electrochem. Soc*. **2001**, *148*, A960.
(10) Yamada, A.; Kudo, Y.; Liu, K.-Y. *J. Electrochem. Soc*. **2001**, *148*, A1153.
(11) Yamada, A.; Kudo, Y.; Liu, K.-Y. *J. Electrochem. Soc*. **2001**, *148*, A747.
(12) Yonemura, M.; Yamada, A.; Takei, Y.; Sonoyama, N.; Kanno, R. *J. Electrochem. Soc.* **2004**, *151*, A1352.
(13) Piana, M.; Cushing, B. L.; Goodenough, J. B.; Penazzi, N. *Solid State Ionics* **2004**, *175*, 233.
(14) Delacourt, C.; Laffont, L.; Bouchet, R.; Wurm, C.; Leriche, J.-B.; Morcrette, M.; Tarascon, J.-M.; Masquelier, C. *J. Electrochem. Soc.* **2005**, *152*, A913.
(15) Li, G.; Azuma, H.; Tohda, M. *Electrochem. Solid State Lett.* **2002**, *5*, A960.
(16) Yamada, A.; Yonemura, M.; Takei, Y.; Sonoyama, N.; Kanno, R. *Electrochem. Solid State Lett.* **2005**, *8*, A55.
(17) Rissouli, K.; Benkhouja, K.; Ramos-Barrado, J. R.; Julien, C. *Mater. Sci. Eng.* **2003**, *B98*, 185.
(18) Eventoff, W.; Martin, R.; Peacor, D. R. *Am. Mineral*. **1972**, *57*, 45.
(19) Dokko, K.; Shiraishi, K.; Kanamura, K. *J. Electrochem. Soc.* **2005**, *152*, A2199.
(20) Wizansky, A. R.; Rauch, P. E.; Disalvo, F. J. *J. Solid State Chem.* **1989**, *81*, 203.

radiation, collected at 0.03 step widths over a 2θ range from 10 to 120°. Structural parameters were refined by Rietveld analysis using the computer program RIETAN 2000.[21] Neutron diffraction data were obtained with a time-of-flight neutron powder diffractometer, VEGA, at the KENS pulsed spallation neutron source at the National Laboratory for High Energy Accelerator (KEK, Tsukuba, Japan). The specimen (of ca. 5 g) was contained in a cylindrical vanadium cell (radius 5 mm, height 55 mm, thickness 200 μm). Structural parameters were refined using the RIETAN-2001T package.[22]

Total neutron scattering measurements were performed using a high-intensity total scattering spectrometer, HIT-II, at KENS. Samples were contained in a 8 mmϕ × 40 mm cylindrical vanadium cell. Raw data were corrected for contributions from the background, empty container, attenuation, and multiple scattering before normalizing to the scattering from the vanadium rod to give the structure factor, $S(Q)$, where the modulus of the scattering vector $Q = 4\pi(\sin\,\theta)/\lambda$. The atomic density values used in the data corrections were calculated from the effective mass densities ρ_{eff} (weight of sample divided by volume of container) and mean atomic weights. The radial distribution function, RDF(r), was obtained from the Fourier transformation of $S(Q)$.

Magnetization was measured by a superconducting quantum interference device magnetometer (Quantum Design, MPMS2) between 5 and 300 K in a field of 1 kOe. Measurements were performed with a heating rate of 1.5 K/min after cooling in zero field (ZFC) and then measured again during a cooling rate of 1.5 K/min under a constant magnetic field of 1000 Oe (field cooling, FC).

For electrochemical tests, self-assembled $\mathrm{LiMPO_4}$ (M = Fe, Mn)/carbon composites were synthesized on the basis of the carbon coating concept first proposed by Ravet et al.;[3] the synthesis was nearly identical with that described above except for an initial addition of porous conductive carbon (LION, ECP) with an estimated amount of 10 wt % in the final $\mathrm{LiMPO_4}$/C composite.[6] The sintering temperature chosen was 600 °C to minimize particle growth without sacrificing purity.[2]

Electrochemical measurements were performed using a stainless steel cell (HS test cell, Hosen Co.). The electrolyte was 1 M $\mathrm{LiPF_6}$ in 3:7 ethylene carbonate/diethyl carbonate (Mitsubishi Petrochemical, battery grade). The counter electrode composed of lithium metal foil was a disk 15 mm in diameter and 0.30 mm thick. The separator was a polypropylene filter sheet. The working electrode was a 10:1 (w/w) mixture of cathode composite/polyvinylidene fluoride. The mixture was added to a minimal amount of *N*-methylpyrrolidon, and the slurry was cast on Al film. After drying at 120 °C, a circular disk was punched for use. The active materials layer was 70 μm thick with a loading of about 10 mg/cm^2. All electrochemical tests were performed at 25 °C using a potentio/galvanostat HA-502 (Hokuto Denko) and a TOSCAT-3100 battery tester (Toyo System).

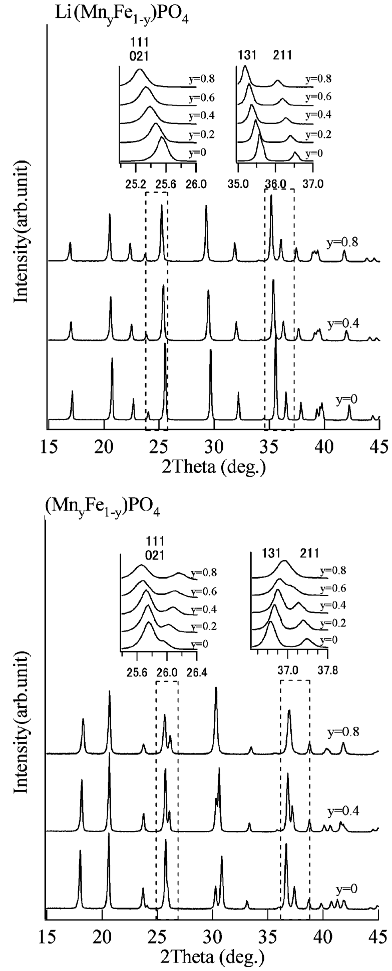

Figure 2. XRD profiles measured for synthetic Li(Mn$_y$Fe$_{1-y}$)PO$_4$ and (Mn$_y$Fe$_{1-y}$)PO$_4$.

Results and Discussion

X-ray/Neutron Diffraction Profiles. XRD profiles measured for the synthetic phases of Li(Mn$_y$Fe$_{1-y}$)PO$_4$ ($0 \le y \le 1$) and (Mn$_y$Fe$_{1-y}$)PO$_4$ ($0 \le y \le 0.8$) are shown in Figure 2. For the Li(Mn$_y$Fe$_{1-y}$)PO$_4$ series, the orthorhombic lattice expands in an isotropic manner as a function of the Mn content y, because the diffraction profiles are similar except for the degree of continuous shift of the diffraction angles as represented in Figure 2 using (111), (021), (131), and (211) diffraction peaks. In contrast, profiles for the (Mn$_y$Fe$_{1-y}$)PO$_4$ series show significant changes as a function of the $\mathrm{Mn^{3+}}$ content y, indicating an anisotropic change in orthorombicity induced by $\mathrm{Mn^{3+}}$ incorporation. The pure $\mathrm{MnPO_4}$ phase with *Pnma* structure was excluded from consideration for the angle- or time-resolved diffraction experiment because of its metastable nature.[9,10] The significant loss of long-range order in the $\mathrm{MnPO_4}$ phase was induced during the 3+/2+ bi-phasic partial oxidation of $\mathrm{Li_xMnPO_4}$.[9] During further delithiation to achieve $x = 0$, gradual transformation was induced to form the hydrated phase, $\mathrm{MnPO_4{\cdot}H_2O}$, or amorphous phase, upon storage under a wet or dry atmosphere, respectively.[9,10] This phase instability was first reported by Yamada and Chung[9] and was considered to be caused by elastic energy accumulated inside the lattice. In general, electronic stabilization energy is proportional to the distortion, whereas elastic energy loss is proportional to the square or higher order of the distortion. At $y > 0.8$ in the (Mn$_y$Fe$_{1-y}$)PO$_4$ series, a penalty in elastic energy with a large local Jahn−Teller deformation of the $\mathrm{Mn^{3+}O_6}$ octahedra could not be compensated for by a gain in electronic energy, which stabilizes the cooperative deformation in the $y < 0.8$ region. This mechanism is supported by recent reports, and major structural databases such as the Inorganic Crystal Structure Database (ICSD) and Cambridge Structural Data-

---

[21] Izumi, F. In *The Rietveld Method*; Young, R. A., Ed.; Oxford University Press: Oxford, 1993; Chapter 13.

[22] Ohta, T.; Izumi, F.; Oikawa, K.; Kamiyama, T. *Physica B (Amsterdam)* **1997**, *234−236*, 1093.

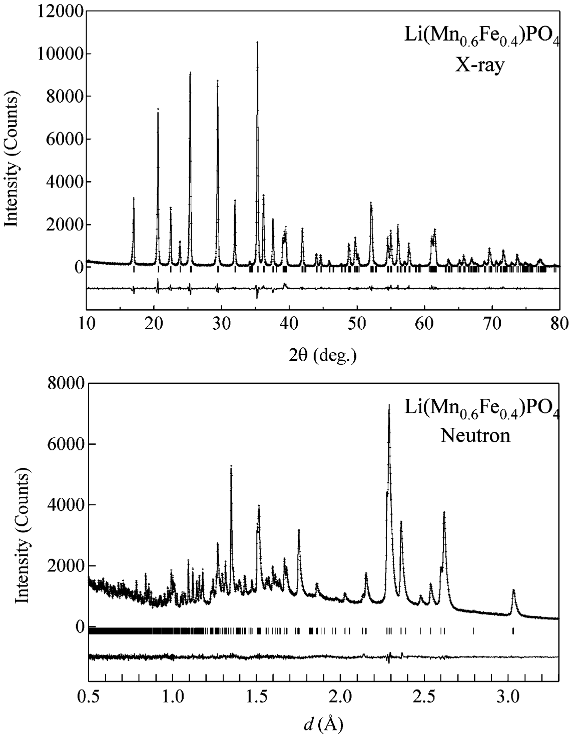

Figure 3. Rietveld refinement pattern of the X-ray and neutron diffraction data for $Li(Mn_{0.6}Fe_{0.4})PO_4$ at room temperature. The observed intensity data are shown by dots; the solid line overlying them is the calculated intensity. Vertical markers below the diffraction patterns indicate positions of possible Bragg reflections. Differences between the observed and calculated intensities are plotted as D_{yi} at the same scale.

Table 1. Rietveld Refinement Results for $Li(Mn_{0.6}Fe_{0.4})PO_4$ with X-ray Diffraction Data[a]

atom	site	*g*	*x*	*y*	*z*	*B* (Å)
Li	4a	1	0	0	0	1.0
Fe, Mn	4c	1	0.2819(9)	0.25	0.9726(2)	0.6
P	4c	1	0.0939(1)	0.25	0.4129(3)	0.6
O1	4c	1	0.0952(4)	0.25	0.7367(8)	1.0
O2	4c	1	0.4563(4)	0.25	0.2116(8)	1.0
O3	8d	1	0.163(3)	0.0489(5)	0.2792(5)	1.0

[a] $a = 10.3960(1)$ Å, $b = 6.060\ 79(7)$ Å, c=4.723 03(6) Å. $R_{wp} = 9.96$, $R_p = 7.77$, $S = R_{wp}/R_e = 1.65$, $R_I = 1.54$, $R_F = 0.79$.

Table 2. Rietveld Refinement Results for $Li(Mn_{0.6}Fe_{0.4})PO_4$ with Neutron Diffraction Data[a]

atom	site	*g*	*x*	*y*	*z*	*B* (Å)
Li	4a	1	0	0	0	1.19(8)
Fe, Mn	4c	1	0.2850(5)	0.25	0.971(1)	0.62(9)
P	4c	1	0.0936(1)	0.25	0.4130(2)	0.25(2)
O1	4c	1	0.0972(1)	0.25	0.7351(3)	0.45(2)
O2	4c	1	0.4567(1)	0.25	0.2089(3)	0.50(2)
O3	8d	1	0.1633(1)	0.0484(1)	0.2802(2)	0.49(1)

[a] $a = 10.4011(1)$ Å, $b = 6.064\ 22(7)$ Å, $c = 4.724\ 55(5)$ Å. $R_{wp} = 2.73$, $R_p = 2.20$, $S = R_{wp}/R_e = 1.24$, $R_I = 1.13$, $R_F = 0.97$.

base (CSD) do not list as stable *Pnma* structures for pure $MnPO_4$.[13] The pure crystalline $MnPO_4$ phase has not yet been isolated.

As shown in Figure 2, all samples other than $MnPO_4$ were well-crystallized and indexed by the single-phase orthorhombic *Pnma*. Rietveld refinement indicated good reliability indices of $R_{wp} < 7.5$ and $S = R_{wp}/R_e < 1.4$ as shown in Figure 3 and Table 1 for $Li(Mn_{0.6}Fe_{0.4})PO_4$. Consistency between X-ray (Table 1) and neutron (Table 2) diffraction experiments was reasonable enough to discuss the local crystal geometry based on X-ray diffraction data in the later sections. No impurity phases appeared to exist within the diffraction profiles. However, oxidized or reduced impurities segregated as nanoparticles or existing as a surface-thin layer on the particle are easily formed during the sintering process and cannot be detected by diffraction measurements.[2,8,19] These phases are known to strongly influence cathode performance in both positive and negative ways and should be carefully characterized. Magnetic behavior as well as Mössbauer and Raman spectroscopy are very sensitive to the valence state and ferro- or ferrimagnetic impurities such as Fe, Fe_2O_3, Fe_3O_4, $Li_3Fe_2(PO_4)_3$, Fe_2P, Fe_3P, and $Fe_{75}P_{15}C_{10}$.[2,8,19] For all samples used in this study, pure antiferromagnetic signals inherent to the olivine phases were measured.

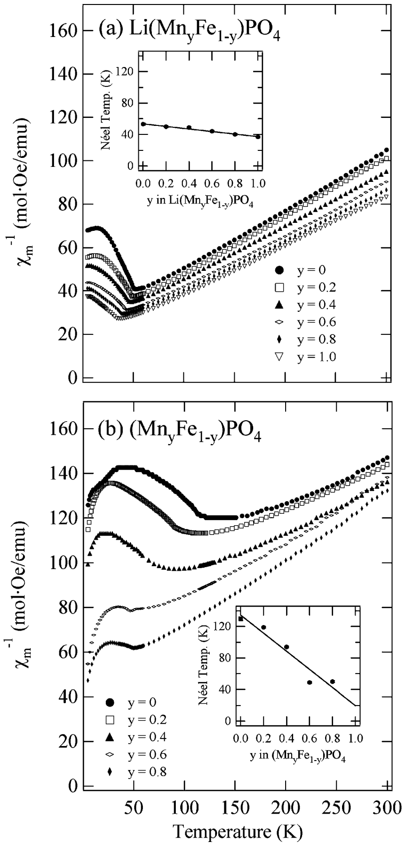

Figure 4. Temperature dependence of the inverse magnetic susceptibility (ZFC) for (a) $Li(Mn_yFe_{1-y})PO_4$ and (b) $(Mn_yFe_{1-y})PO_4$.

Magnetic Susceptibility. Figure 4 shows the temperature dependence of inverse magnetic susceptibility as measured for samples sintered at 700 °C. All samples showed typical behavior for an antiferromagnetic ground state below the Néel temperature, reported as collinear for stoichiometric $LiFePO_4$ ($T_N = 52$ K), $LiMnPO_4$ ($T_N = 35$ K), and $FePO_4$ ($T_N = 125$ K) phases, but with different spin orientations.[23,24] Values for effective magnetic moment μ_{eff} are calculated by

$$\chi_m^{-1} = (T - \theta)/C_m \qquad \mu_{eff} = \sqrt{8C_m}\mu_B$$

where θ is the Weiss temperature, C_m is the Curie constant, and μ_B is the Bohr magneton. The value of C_m was estimated by the least-squares linear plot in the temperature range of

---

(23) Santoro, R. P.; Newman, R. E. *Acta Crystallogr.* **1967**, *22*, 344.

(24) Rosse, G.; Rodriguez-Cavajal, J.; Patoux, S.; Masquelier, C. *Chem. Mater.* **2003**, *15*, 4082.

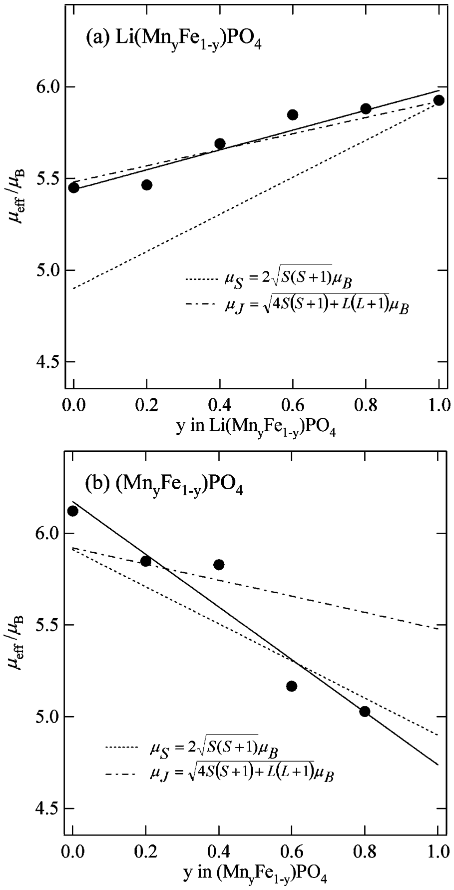

Figure 5. Experimental magnetic moment μ_{eff} for (a) Li(Mn_yFe_{1-y})PO_4 and (b) (Mn_yFe_{1-y})PO_4 with the theoretical lines based on the total magnetic moment $\mu_J = [4S(S+1) + L(L+1)]^{1/2}\mu_B$ and on the spin-only magnetic moment $\mu_S = 2[S(S+1)]^{1/2}\mu_B$.

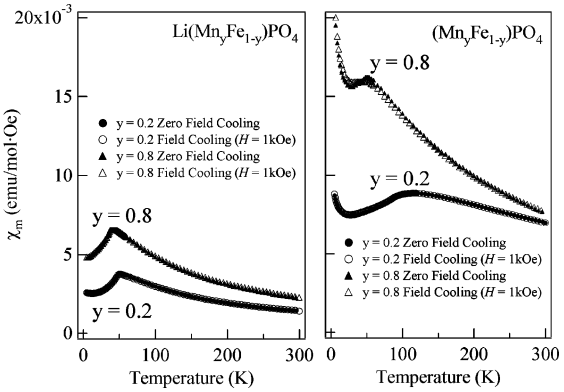

Figure 6. Temperature dependence of magnetic susceptibility for ZFC and FC processes.

200−300 K. The effect on the Néel temperature, T_N, is much larger in the (Mn_yFe_{1-y})PO_4 system (ca. 125 K for $y = 0$ to ca. 50 K for $y = 0.8$) than in the Li (Mn_yFe_{1-y})PO_4 system (ca. 52 K for $y = 0$ to ca. 35 K for $y = 1$), as might be expected from the larger change in the crystallographic geometry, the details of which will be discussed in a later section.

In the divalent Li(Mn_yFe_{1-y})PO_4 system, the experimental effective magnetic moment μ_{eff} followed the theoretical line based on the total magnetic moment $\mu_J = [4S(S + 1) + L(L + 1)]^{1/2}\mu_B$ but not on the spin-only magnetic moment $\mu_S = 2[S(S + 1)]^{1/2}\mu_B$, as shown in Figure 5a. Usually, S is the quantum number used to describe the magnetic properties of three-dimensional transition metals. However, it is known that there is a contribution from the angular momentum of the minority spin in the t_{2g} orbital under O_h symmetry, and $J = S + L$ is the quantum number used for the d^4 or d^5 low-spin configuration and d^6 or d^7 high-spin configuration. Although local symmetry is lowered to C_s in the present case, the divalent Fe in $LiFePO_4$ has a d^6 high-spin $^5D_4$ ($S = 2$, $L = 2$, $J = 4$) configuration with single minority spin, while the divalent Mn in $LiMnPO_4$ has a d^5 high-spin $^6S_{5/2}$ ($S = 5/2$, $L = 0$, $J = 5/2$) configuration with no minority spin. High-spin configuration of the transition metal M in the $LiMPO_4$ and MPO_4 phases has been suggested by the density of state obtained by the first principle calculations.[9,25−27]

According to these results, the experimental effective magnetic moment in the trivalent (Mn_yFe_{1-y})PO_4 system should follow the spin-only magnetic moment μ_S rather than the total magnetic moment μ_J, because both Mn^{3+} with a d^4 high-spin $^5D_0$ ($S = 2$, $L = 2$, $J = 0$) configuration and Fe^{3+} with a d^5 high-spin $^6S_{5/2}$ ($S = 5/2$, $L = 0$, $J = 5/2$) configuration have no minority spin in the orbital with a primarily t_{2g}-like character. The overall trend of the experimental μ_{eff} in Figure 5 is consistent with this; it follows the theoretical value from the spin-only assumption μ_S, particularly when the manganese content y is large. However, μ_{eff} shows larger values than the theoretical ones in the region of small y. The origin of this deviation is not clear and may result from linear plot estimation within the narrow temperature range of 200−300 K and/or indirect melting into the paramagnetic state through incommensurately modulated phases as observed in $LiNiPO_4$.[28]

Magnetization measurements revealed similar susceptibility curves independent of ZFC or FC processes for all samples with no parasite signals (Figure 6), which guarantees the high quality of samples with no ferro- or ferrimagnetic impurity or domains as have often detected by Mössbauer or Raman spectroscopy.[2,19] However, samples sintered at temperatures less than 500 °C showed strong signals for spontaneous magnetization upon FC, consistent with previous Mössbauer or Raman measurements.[2,19] The following electrochemical and structural studies are based on the synthetic high-quality sample sintered at 600−700 °C; therefore, the results should be very reliable.

Electrochemical Properties. The trickle charge−discharge curves measured for the $Li_x(Mn_yFe_{1-y})PO_4$ system ($y = 0$, 0.2, 0.4, 0.6, 0.8, 1) at a $C/20$ rate are shown in Figure 7. Under such slow rate conditions, the two redox plateaus, Mn^{3+}/Mn^{2+} at 4.1 V and Fe^{3+}/Fe^{2+} at 3.4 V, are distinguishable and appear as functions of the initial Mn/Fe composition ratio. A clear potential bump in charge−discharge curves between the two corresponds to a distinctive line, $x = y$ in the (x, y) phase map in the $Li_x(Mn_yFe_{1-y})PO_4$ system with metastable region close to the point $(x, y) = (0, 1)$.[10] As recognized by the increasing polarization in the 4.1

---

(25) Zhou, F.; Kang, K.; Maxisch, T.; Ceder, G.; Morgan, D. *Solid State Commun.* **2004**, *132*, 181.

(26) Tang, P.; Hortzwarth, N. A. W. *Phys. Rev. B* **2003**, *68*, 165107.

(27) Xu, Y.-N.; Ching, W. Y.; Chiang, Y.-M. *J. Appl. Phys.* **2004**, *95*, 6583.

(28) Vaknin, D.; Zarestky, J. L.; Rivera, J. P.; Schmid, H. *Phys. Rev. Lett.* **2004**, *92*, 207201.

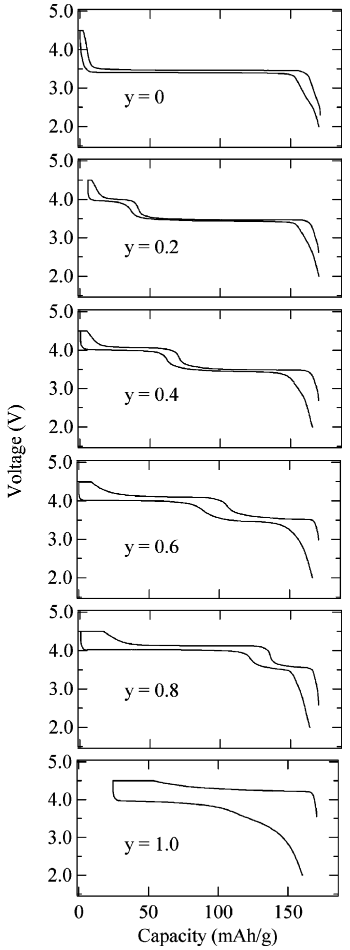

Figure 7. Trickle charge−discharge curves measured for the $Li_x(Mn_yFe_{1-y})PO_4$ system ($y = 0$, 0.2, 0.4, 0.6, 0.8, 1) at a $C/20$ rate.

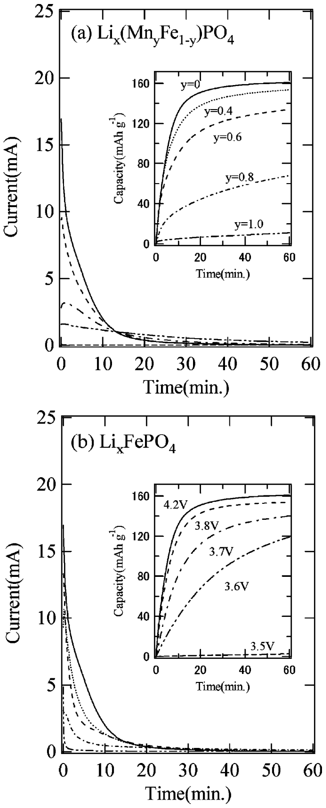

Figure 8. (a) Current responses to stepwise anodic overvoltages of 4.2 V vs Li/Li^+ applied to $Li(Mn_yFe_{1-y})PO_4$. (b) Current response to stepwise anodic overvoltages of 3.5−4.2 V vs Li/Li^+ applied to $LiFePO_4$. Integrated current responses represent time-dependent anodic capacity consumption.

V plateau, electrochemical activity of Mn^{3+}/Mn^{2+} decreases with an increase in manganese content.

Unusual loss of electrochemical activity of the Mn^{3+}/Mn^{2+} redox reaction in the olivine structure was more evident under the critical experimental conditions requiring rapid kinetics. Current responses to 60-min stepwise constant voltage of 4.2 V versus Li/Li^+ at 25 °C were integrated to give time-dependent capacity consumption and are summarized in Figure 8a. This experimental condition is severe for the Mn^{3+}/Mn^{2+} redox reaction in terms of the weak electrochemical driving force under the small anodic overvoltage of about 0.15 V and the very short reaction time of 60 min. Even at such a short time reaction, $LiFePO_4$ exhibits rapid kinetics in lithium extraction and consumes most of its theoretical capacity (170 mA·h/g) within 10−20 min, whereas the decrease in total capacity consumption is precipitous when the iron is partially substituted by manganese, and Li_xMnPO_4 possessed negligible activity.

It is apparent that, in addition to the inherent abnormally slow kinetics of Mn^{3+}/Mn^{2+}, the larger anodic overvoltage applied for Fe^{3+}/Fe^{2+} (ca. 0.7 V) than for Mn^{3+}/Mn^{2+} (ca. 0.1 V) under a constant voltage of 4.2 V versus Li/Li^+ significantly enhanced the reaction speed and is one reason for the large kinetic difference observed in Figure 8a. On the basis of the conventional belief that rate difficulties in Li_xFePO_4 materials are due to electron conductivity limitations and the first principle calculation supporting high intrinsic ionic conductivity in the olivine structure,[29] it is reasonable that the overpotential provides the external electrochemical power to give motional energy to the polaronic electron/hole system. The anodic overpotential of ∼700 meV versus Fe^{3+}/Fe^{2+} given in Figure 8 is slightly larger than the binding energy measured for polaron localization in $LiFePO_4$ (∼390−500 meV) and can facilitate polaron motion, whereas the small overpotential of ∼150 meV to Mn^{3+}/Mn^{2+} is not effective compared with the much larger polaron localization energy of $LiMnPO_4$ (∼650−1000 meV). The anodic kinetic enhancement of Li_xFePO_4 was a strong function of the applied overvoltage in the region of 3.4−3.8 V (anodic overvoltage of 0−400 mV), while the effect showed abrupt saturation at the applied voltage of >3.8 V (anodic overvoltage of >400 mV), as shown in Figure 8b. In a situation allowing frequent and facile motion of electrons and lithium ions inside the bulk,[30] electrode/electrolyte interfacial charge movement with disolvation may become rate limiting as has been discussed on a conventional metallic electrode as Li_xCoO_2 or Li_xC.[31,32] The binding energy for polaron localization in Li_xFePO_4 is competitive with the disolvation energy.

---

(29) Morgan, D.; Van der Ven, A.; Ceder, G. *Electrochem. Solid State Lett.* **2004**, *7*, A30.

(30) Yamada, A.; Koizumi, H.; Sonoyama, N.; Kanno, R. *Electrochem. Solid State Lett.* **2005**, *8*, A409.

(31) Abe, T.; Fukuda, H.; Iriyama, Y.; Ogumi, Z. *J. Electrochem. Soc.* **2004**, *151*, A1120.

(32) Menetrier, M.; Saadoune, I.; Levasseur, S.; Delmas, C. *J. Mater. Chem.* **1999**, *9*, 1135.

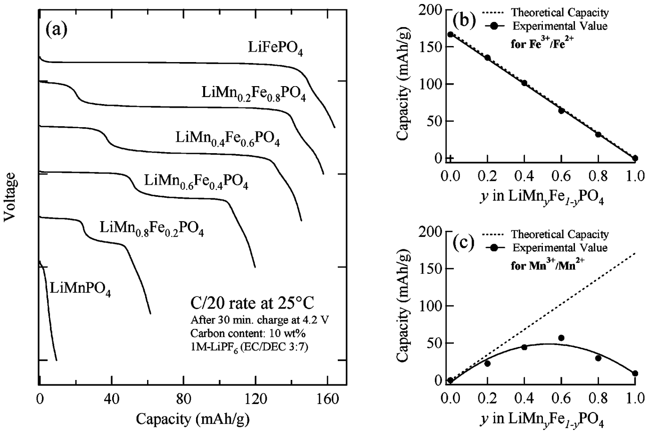

Figure 9. (a) Galvanostatic discharge curves measured at the *C*/20 rate after a 30-min potentiostatic oxidation at 4.2 V vs Li/Li$^+$ for Li(Mn$_y$Fe$_{1-y}$)PO$_4$. (b) Discharge capacity obtained at the 3.4 V plateau for the Fe^{3+}/Fe^{2+} region. (c) Discharge capacity obtained at the 4.1 V plateau for the Mn^{3+}/Mn^{2+} redox region. The dashed lines in parts b and c are theoretically capacity dependent on the Mn content *y*.

Table 3. Rietveld Refinement Results for (Mn$_{0.8}$Fe$_{0.2}$)PO$_4$[a]

atom	site	*g*	*x*	*y*	*z*	*B* (Å)
Fe, Mn	4c	1	0.2826(8)	0.25	0.9231(2)	0.6
P	4c	1	0.0957(1)	0.25	0.3917(2)	0.6
O1	4c	1	0.1205(4)	0.25	0.7089(8)	1.0
O2	4c	1	0.4406(9)	0.25	0.1557(3)	1.0
O3	8d	1	0.1649(1)	0.0436(2)	0.2436(7)	1.0

[a] $a = 9.6629(2)$ Å, $b = 5.8841(1)$ Å, $c = 4.7770(1)$ Å. $R_{wp} = 7.74$, $R_p = 5.84$, $S = R_{wp}/R_e = 1.4884$, $R_I = 0.91$, $R_F = 0.65$.

The subsequent galvanostatic discharge profiles at a *C*/20 rate after the 30-min potentiostatic oxidation at 4.2V versus Li/Li$^+$, shown in Figure 8, are summarized in Figure 9a. Consistent with the data in Figure 8, the total capacity decrease is not monotonic but abrupt at $y > 0.6$.[9] However, on closer inspection, most of the electrochemical activity loss was in Mn^{3+}/Mn^{2+}, while the Fe^{3+}/Fe^{2+} capacity always followed the theoretical line, as shown in Figure 9b,c. In addition, the Mn^{3+}/Mn^{2+} capacity followed the theoretical line in the region of small *y*, followed by a gradual deviation near $y = 0.6$ and a precipitous decrease at $y > 0.7$, finalized by total capacity disappearance at $y = 1$. Therefore, the electrochemical activity of Mn^{3+}/Mn^{2+} in Li$_x$(Mn$_y$Fe$_{1-y}$)PO$_4$ is not solely determined by the inherent negligible activity of Mn^{3+}/Mn^{2+} in Li$_x$MnPO$_4$ but also strongly dependent on the amount of Fe ions coexisting in octahedral sites.

Geometries and Interactions. The X-ray diffraction profiles were refined to the stoichiometric compositions with no impurity phases, although several types of cation disorder and vacancy modes, such as Li$_{1-2x}$M$^{2+}{}_x$MPO$_4$ and Li$_{1-3x}$M$^{3+}{}_x$MPO$_4$ or their delithiated phases, were considered. Rietveld refinement results for the X-ray diffraction data measured for (Mn$_{0.8}$Fe$_{0.2}$)PO$_4$ are summarized in Table 3. The bond angles and bond lengths in MO$_6$ and PO$_4$ polyhedra were obtained using the positional parameters and lattice constants in Table 3 and are summarized in Table 4.

The analysis was performed for other compositions on the two solid−solution lines of trivalent (Mn$_y$Fe$_{1-y}$)PO$_4$ ($y = 0$, 0.2, 0.4, 0.6) and divalent Li(Mn$_y$Fe$_{1-y}$)PO$_4$ ($y = 0$, 0.2, 0.4, 0.6, 0.8, 1). Changes in the M−O bond lengths in MO$_6$ octahedra and the P−O bond lengths in PO$_4$ tetrahedra are summarized in Figures 10 and 11. Introducing Mn ions into the 4c site did not significantly change the local geometry of M^{2+}O$_6$ octahedra and PO$_4$ tetrahedra. The M^{2+}−O bond lengths showed an isotropic linear increase as a function of manganese content *y* and can be explained simply by the difference in the ionic radii of the high-spin Mn^{2+} (0.97 Å) and high-spin Fe^{2+} (0.92 Å). The rigid small PO$_4$ polyanion with a covalent P−O bond is not surprising. M^{3+}O$_6$ octahedra become severely distorted with an increase in the Jahn−Teller active Mn^{3+} ions with selective strong elongation of the M^{3+}−O3′ distance and weak shrinkage of other M^{3+}−O1, M^{3+}−O2, and M^{3+}−O3 bond lengths. Definitions for the notations O1, O2, O3, and O3′ are given in Figures 1 and 12, where the local networking geometry of one MO$_6$ octahedron and four PO$_4$ tetrahedra is given. As can be seen in Figure 1, the Fe site has C_s symmetry with a mirror plane perpendicular to the paper, as shown in Figure 12a, which passes through O1 and O2. The six Fe−O bonds differ by as much as 0.2 Å in length and are categorized into four shells (2O3 + 2O3′ + 1O1 + 1O2). The oxygen atoms can roughly be grouped into ‘‘axial” (O1, O2) and ‘‘equatorial” (O3, O3′) types. The angle O1−Fe−O2 is roughly 180° with

Table 4. Selected Interatomic Distances (Å) and Angles (deg) in Mn$_{0.8}$Fe$_{0.2}$PO$_4$

M[a]	O1	O2	O3	O3	O3′	O3′
O1	1.870(5)	177.1(2)	88.7(2)	88.7(2)	87.0(9)	87.0(9)
O2	3.75(8)	1.889(0)	92.7(0)	92.7(0)	90.4(7)	90.4(7)
O3	2.70(3)	2.52(9)	1.994(3)	120.0(7)	87.3(4)	152.1(6)
O3	2.70(3)	2.52(9)	3.45(5)	1.994(3)	152.(6)	87.3(4)
O3′	2.86(0)	2.81(0)	3.45(5)	4.13(1)	2.261(2)	64.9(6)
O3′	2.86(0)	2.81(0)	4.13(1)	3.45(5)	2.42(8)	2.261(2)

P[b]	O1	O2	O3′	O3′
O1	1.534(4)	107.6(0)	112.4(3)	112.4(3)
O2	2.46(0)	1.515(0)	110.9(8)	110.9(0)
O3′	2.56(8)	2.52(9)	1.556(3)	102.5(7)
O3′	2.56(8)	2.52(9)	2.42(8)	1.556(3)

[a] ⟨M−O⟩ = 2.045(2) Å; predicted = 2.025 Å; $\Delta_d = 6.35 \times 10^{-3}$. ⟨O−M−O′⟩ = 89.8092°; $\Delta_\varphi = 1.59 \times 10^{-2}$. [b] ⟨P−O⟩ = 1.541(5) Å; predicted = 1.55 Å; $\Delta_d = 1.60 \times 10^{-3}$. ⟨O−P−O′⟩ = 109.485°; $\Delta_\varphi = 1.01 \times 10^{-3}$.

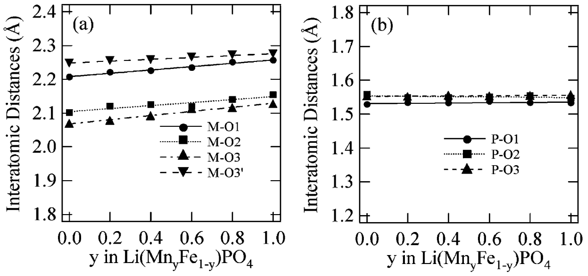

Figure 10. Interatomic distances for (a) M−O and (b) P−O for Li(Mn$_y$Fe$_{1-y}$)PO$_4$.

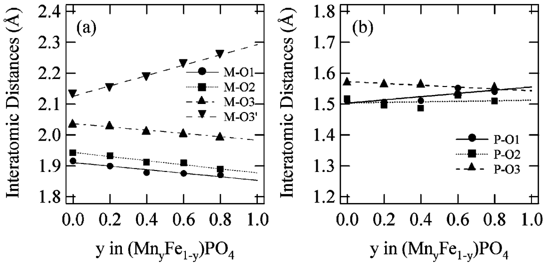

Figure 11. Interatomic distances for (a) M−O and (b) P−O for (Mn$_y$Fe$_{1-y}$)PO$_4$.

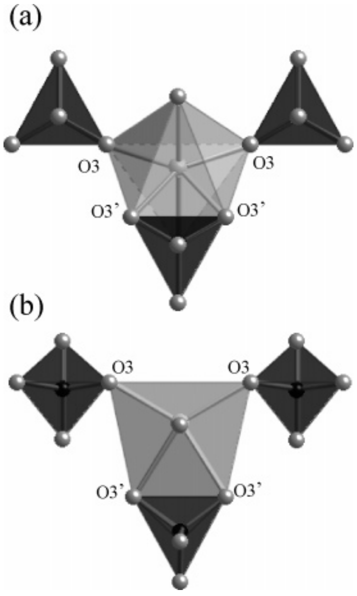

Figure 12. Local networking geometry of MO_6 octahedra and PO_4 tetrahedra in $LiMPO_4$ in projection along (a) [001] and (b) the principal axis of the MO_6 octahedra.

an axial direction. On the plane perpendicular to the O1−Fe−O2 line, O3−Fe−O3′ roughly forms a ‘‘scissors” structure with O−Fe−O angles far from 90°. The MO_6 octahedra share their edges through two O3′ atoms with one PO_4 tetrahedron and share corners through O1, O2, and two O3 atoms with four PO_4 tetrahedra.

Usually, the Jahn−Teller distortion of MO_6 octahedra (O_h symmetry) shows an elongation of the two axial (c direction) bond lengths and shrinkage of the four equatorial (a direction) bond lengths, to give a general expression as $c/a > 1$. However, the Jahn−Teller effect in the MO_6 octahedra with barely ionized M ions tends to yield an equatorial/axial ratio inversion of $c/a < 1$, where the two axial bond lengths shrink and another four equatorial bond lengths expand. Such an inversion is typically observed for strongly ionized epidote or perovskite materials, where the metastable $c/a < 1$ configuration is stabilized in a crystal to prevent the penalty in energy required to distort the structure from the metastable $c/a < 1$ structure to the stable $c/a > 1$.[33] The $(Mn_yFe_{1-y})PO_4$ series evidently belongs to the latter case of $c/a < 1$ because the transition metals are strongly ionized by the M−O−P inductive effect. As indicated by the overall trend shown in Figure 11, elongation along the equatorial 2O3−M−2O3′ plane is clear, while the O1−M−O2 axial direction shows weak shrinkage. However, the elongation was observed only for M^{3+}−O3′, whereas M^{3+}−O3 shows weak shrinkage. It seems that the edge-sharing geometry of $M^{3+}O_6$ and PO_4 polyhedra fixes the shared O3′−O3′ interatomic distance and gives rise to selective strong elongation of the M^{3+}−O3′ distance in the 2O3−M−2O3′ equatorial plane.

We focused on the extent of the local structural changes in MO_6 octahedra along the two solid−solution lines of $Li(Mn_yFe_{1-y})PO_4$ and $(Mn_yFe_{1-y})PO_4$ and compared them with those of the unit-cell dimensions. These data are summarized in Figure 13, with a percent expression for the changes in M−O bond lengths and orthorhombic lattice constants. Along the divalent line, there was no significant difference between the isotropic deformations in the orthorhombic unit cell and those in the MO_6 octahedra (<3%). In contrast, the overall distortion of the MO_6 octahedra with M = Mn^{3+} is about 12% at maximum, much larger than the corresponding change in the unit-cell orthorombicity (ca. 4%). These results are consistent with the significant damping in the extended X-ray absorption fine structure spectra for the $(Mn_yFe_{1-y})PO_4$ series reported previously.[10] As a quan-

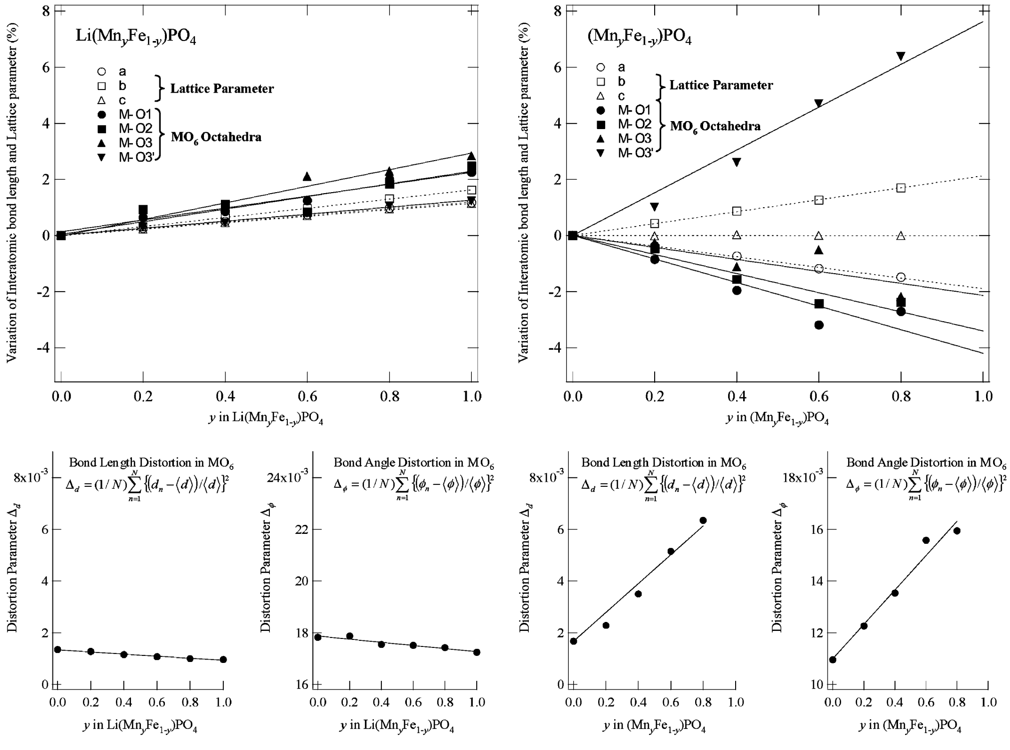

Figure 13. Percent expression of variation in interatomic bond lengths (solid lines) and lattice parameters (dashed lines) for $Li(Mn_yFe_{1-y})PO_4$ and $(Mn_yFe_{1-y})PO_4$. The change in the distortion parameters of MO_6 octahedra for bond lengths and bond angles also is shown.

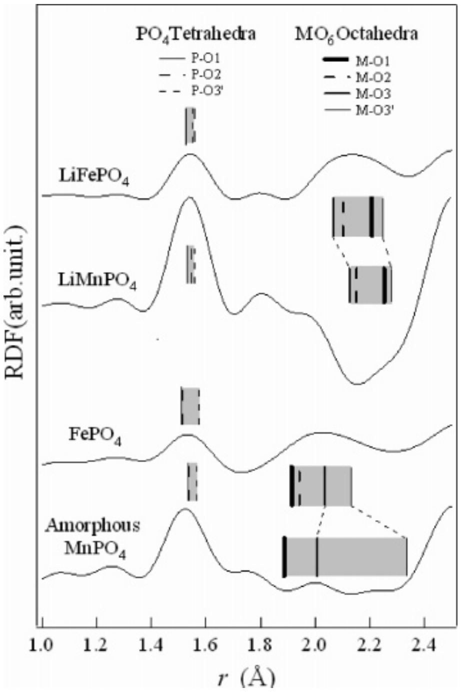

Figure 14. Radial distribution function (RDF) for $LiFePO_4$, $FePO_4$, $LiMnPO_4$, and amorphous $MnPO_4$ obtained by neutron total diffraction. Rectangular bars represent the interatomic bond lengths obtained by the Reitveld refinement for $LiFePO_4$, $FePO_4$, and $LiMnPO_4$ and by first principle calculation for amorphous $MnPO_4$. The M−O3 and M−O3′ bond lengths are related to the superexchange interaction and are connected by dashed lines to show the significant change in asymmetry.

titative indicator for the severe $M^{3+}O_6$ local distortion, the following distortion parameters for bond lengths Δ_d and bond angles Δ_ϕ in MO_6 octahedra are defined and are summarized in Figure 13:

$$\Delta_d = \left(\frac{1}{N}\right)\sum_{n=1}^{N}\left(\frac{d_n - \langle d\rangle}{\langle d\rangle}\right)^2 \qquad \Delta_\phi = \left(\frac{1}{N}\right)\sum_{n=1}^{N}\left(\frac{\phi_n - \langle\phi\rangle}{\langle\phi\rangle}\right)^2$$

where $\langle d\rangle$ and $\langle\phi\rangle$ are the average bond length and bond angle, respectively.

The radial distribution functions (RDF) for $LiFePO_4$, $FePO_4$, $LiMnPO_4$, and amorphous $MnPO_4$ obtained by neutron total diffraction are given in Figure 14. These functions aid the understanding of the overall trend in the change in local geometry of the $Li_x(Mn_yFe_{1-y})PO_4$ system. As a result of the difference of the sign in the neutron scattering length, that is, Fe(+9.45), Mn(−3.73), P(+5.13), and O(+5.803), negative peaks for Mn−O correlation and positive peaks for P−O and Fe−O correlations are observed at the corresponding bond distances. To demonstrate this, bond lengths obtained by the Rietveld refinement of X-ray diffraction data for $LiFePO_4$, $FePO_4$, and $LiMnPO_4$ are denoted as rectangular bars in Figure 14. Because no experimental crystallographic data are available for the metastable pure $MnPO_4$ with a *Pnma* structure, we inferred the bond lengths in amorphous $MnPO_4$ from the optimized geometries obtained by the first principle calculation kindly supplied by Morgan and Ceder.[34] Note that the bond lengths based on the calculated optimized geometry are coincident with the line extrapolation toward $y = 1$, as shown in Figure 11. Even in the amorphous phase, local coordination around Mn^{3+} appears to be influenced by the Jahn−Teller effect.[10] Among the four types of M−O bonds in the MO_6 octahedra, the equatorial M−O3 and M−O3′ bonds contribute to the neighboring superexchange interaction as shown in Figure 15 with an MO_4 networking layer. The enhanced asymmetry in the M−O−M superexchange interaction upon oxidation of the manganese system is highlighted by the dashed line in Figure 14, which should influence the antiferromagnetic ground state.

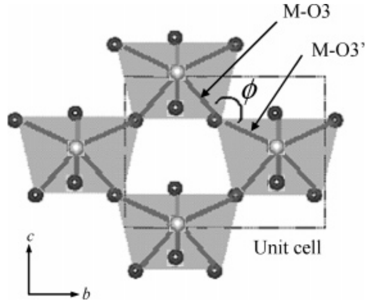

Figure 15. Connection via corner sharing of the MO_6 octahedra in $LiMPO_4$ in projection along [100]. The shared oxygen is O3 for one octahedron but is O3′ for the other octahedra. The bond lengths, M−O3 and M−O3′, and bond angle, ϕ, related to the neighboring superexchange interaction J_1 are denoted.

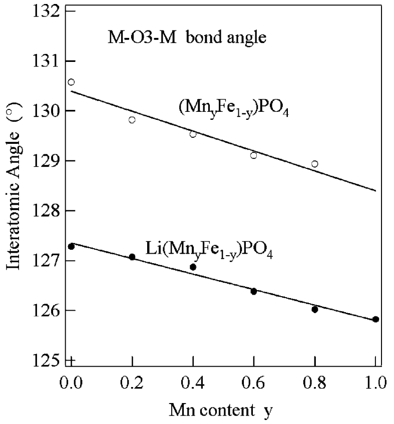

Figure 16. Interatomic angles in the neighboring M−O−M superexchange interaction J_1 for $Li(Mn_yFe_{1-y})PO_4$ and $(Mn_yFe_{1-y})PO_4$.

All samples exhibited the antiferromagnetic magnetic ground state as shown in Figure 4. This is roughly consistent with the Goodenough−Kanamori superexchange rules for the 180° interaction,[35−37] although the M−O−M bond angle on the neighboring intralayer superexchange interaction J_1 largely deviates from 180° and is distributed from 126 to 130° (Figure 16). As shown in Figure 17, the M−O···O−M super-superexchange paths with the O···O in contact through a distance shorter than the van der Waals distance (i.e., 2.8 Å) also should be considered in describing the three-dimensional magnetic ordering in $LiMPO_4$, but these are much weaker as demonstrated by recent spin dimer analysis.[38] In the case where the neighboring intralayer super-

---

(33) Sterns, R. G. J. *Mineral. Mag.* **1966**, *35*, 777.

(34) Morgan, D.; Ceder, G. Personal communication.

(35) Goodenough, J. B. *Phys. Rev. B* **1955**, *100*, 564.

(36) Kanamori, J. *J. Phys. Chem. Solids* **1959**, *10*, 87.

(37) Goodenough, J. B. *Magnetism and the Chemical Bond*; Wiley: Cambridge, MA, 1963.

(38) Dai, D.; Whangbo, M.-H.; Koo, H. J.; Rocquefelte, X.; Jobic, S.; Villesuzanne, A. *Inorg. Chem.* **2005**, *44*, 2407.

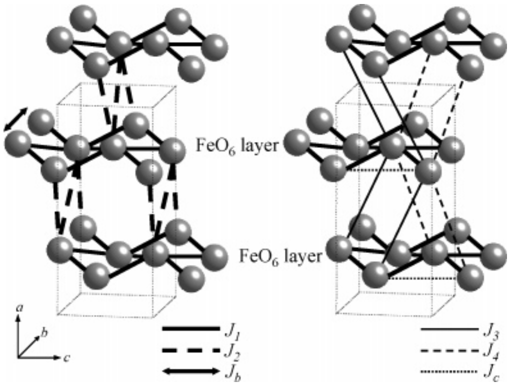

Figure 17. Magnetic interactions in $LiMPO_4$. (a) The dominant neighboring superexchange interaction of intralayer J_1 and the weak but influential super-superexchange interactions of interlayer J_2 and intralayer J_b. (b) Negligible but finite super-superexchange interaction of interlayers J_3 and J_4 and intralayer J_c with the O···O contact shorter than the van der Waals distance (i.e., 2.8 Å).

exchange interaction is dominant, the large difference in T_N is possible by assuming that the $Fe^{3+}-O-Fe^{3+}$ superexchange interaction is much stronger than those of $Mn^{3+}-O-Mn^{3+}$, $Fe^{2+}-O-Fe^{2+}$, and $Mn^{2+}-O-Mn^{2+}$. In the present case, one explanation for the abrupt decrease in T_N in the $(Mn_yFe_{1-y})PO_4$ system is based on the asymmetric superexchange M−O−M interaction, the geometry of which is shown in Figure 15, demonstrating related bond angles and bond lengths. As pointed out by Whangbo et al. for marokite $CaMn_2O_4$, the orbital interactions between the metal centers in a highly asymmetric M−O−M superexchange path are weak.[39] The exchange coupling is proportional to the square of the transfer integral depending sensitively on the amount of partial covalent bonding. Hence, the strength of the spin exchange interactions are governed mainly by the asymmetry of the M−O−M bridges but not by the ∠M−O−M bond angle, as evident in Figures 14 and 16.

Conclusion

Detailed structural and magnetic susceptibility data of the synthetic phase-pure $Li(Mn_yFe_{1-y})PO_4$ and $(Mn_yFe_{1-y})PO_4$ solid solutions have been demonstrated to increase understanding of the unusual loss of electrochemical activity in the Mn-rich phase in $Li_x(Mn_yFe_{1-y})PO_4$. Local geometric changes in $M^{3+}O_6$ octahedra in the $(Mn_yFe_{1-y})PO_4$ series are remarkable because of an unusual synergetic effect in the Jahn−Teller distortion by highly ionized center cations and the edge-shared interconnection with PO_4 tetrahedra, while $M^{2+}O_6$ octahedra and PO_4 tetrahedra do not show any significant anomalous changes. The destabilized antiferromagnetic ground state in $(Mn_yFe_{1-y})PO_4$, $T_N = 130$ K for $y = 0$ to $T_N = 50$ K for $y = 0.8$, may occur as a result of the weakened superexchange interaction by asymmetric $M^{3+}-O-M^{3+}$ bridges.

Acknowledgment. The authors thank D. Morgan and G. Ceder for providing the calculated geometries of the experimentally unavailable pure $MnPO_4$ *Pnma* crystalline phase. This work was financially supported by the TEPCO Research Foundation, the Murata Science Foundation, Grant-in-Aid for Scientific Research from the Ministry of Education, Culture, Sports, Science and Technology of Japan, No. 16350108, and the New Energy and Industrial Technology Development Organization (NEDO) through a research grant to A.Y.

Note Added after ASAP Publication. There was an error in Figure 16 in the version published ASAP January 12, 2006; the corrected version was published ASAP January 23, 2006.

CM051861F

---

(39) Whangbo, M.-H.; Koo, H. J.; Dai, D.; Jung, D. *Inorg. Chem.* **2002**, *41*, 5575.